ACS APPLIED ELECTRONIC MATERIALS

pubs.acs.org/acsaelm

Article

Nanoscale Resistive Switching in Electrodeposited MOF Prussian Blue Analogs Driven by K-Ion Intercalation Probed by C-AFM

Lindiomar Borges de Avila Junior,* Oriane de Leuze, Michael Pohlitz, Marco A. Villena, Ramon Torres-Cavanillas, Colin Ducarme, Anthony Lopes Temporao, Thomas G. Coppée, Anatole Moureaux, Sofiane Arib, Eugenio Coronado, Christian Klaus Müller, Juan Bautista Roldán, Benoît Hackens, and Flavio Abreu Araujo*

Cite This: https://doi.org/10.1021/acsaelm.6c00766

Read Online

ACCESS | Metrics & More | Article Recommendations | Supporting Information

ABSTRACT: K-ion intercalation in Prussian blue analogues (PBAs) is a well-established charge storage mechanism in potassium-ion batteries; here, we demonstrate that this process also responsible for nanoscale resistive switching in PBA-based material. Using conductive atomic force microscopy (C-AFM), we directly visualize and electrically control reversible conductance modulation within sub-100 nm volumes, linking localized K^+ redistribution to Fe^{2+}/Fe^{3+} redox reconfiguration. The switching is polarity-selective, with Prussian white (PW) and Prussian blue (PB) both exhibiting unidirectional resistive switching (URS) at opposite bias polarities, consistent with oxidation- and reduction-driven transport, respectively. These processes are governed by electrically confined ion−electron coupling, where K-ion motion modulates small-polaron hopping within the PBA framework. The switching dynamics are strongly dependent on ionic mobility, with PW sustaining operation up to 200 V/s and PB up to 50 V/s, highlighting the critical role of K-ion concentration in enabling fast redox kinetics. This nanoscale switching mechanism, combined with spatial confinement below 100 nm, enables high-density device integration without interference between them. Moreover, PBAs provide a chemically versatile, earth-abundant platform with tunable ionic and electronic properties, fabricated via a single-step, aqueous, room-temperature process compatible with CMOS technology. This solution-processable approach enables low-temperature fabrication, scalability to large-area substrates, and integration into diverse device architectures. The use of simple salt precursors ensures low-cost manufacturing, while environmentally friendly synthesis and nontoxic, noncontaminating disposal enhance overall sustainability.

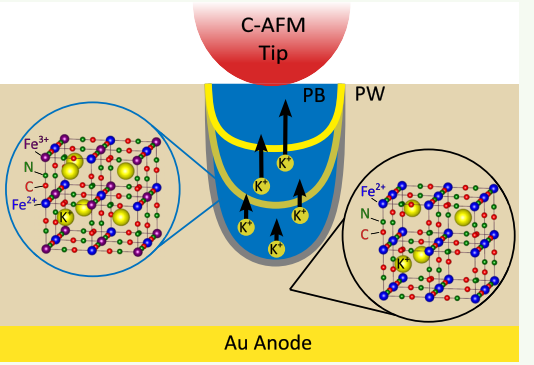

KEYWORDS: *nanoscale resistive switching, Prussian blue analogs, metal−organic framework materials, ion intercalation*

INTRODUCTION

With the rapid expansion of big data and artificial intelligence, the demand for computing technologies capable of delivering high processing speed and low energy consumption has grown dramatically, especially for tasks such as pattern recognition, real-time image processing, and autonomous decision-making.[1−3] However, modern computing still relies predominantly on the traditional von Neumann architecture, in which memory and processing units are physically separated. This structural distinction imposes a severe bottleneck on data throughput and leads to substantial energy losses during frequent memory access.[4−6] In contrast, the human brain performs computation in a massively parallel fashion through densely interconnected networks of neurons and synapses, achieving remarkable efficiency with only a few tens of watts of power consumption.[7,8]

Memristive devices whose conductance can encode a synaptic weight, offer a promising route toward hardware systems that emulate synaptic plasticity and neural information processing.[9−12] Multiple switching mechanisms have been employed to reproduce biological functionality, including conductive filament formation, phase transitions, magnetization switching, and ion migration.[13−16] Among these, ion migration-based memristors are especially attractive because their operation closely mimics the ionic dynamics of biological synapses,

Received: May 13, 2026
Revised: July 27, 2026
Accepted: July 28, 2026

including Ca^{2+} driven plasticity, and because they naturally support analog state evolution.[17,18] These ion-driven effects have inspired the development of battery-like synapses, where electrolytes and electrochemical reactions are used to modulate device conductance at extremely low power.[19,20] However, many of such devices still exhibit millisecond-scale switching times, posing challenges for high-speed neuromorphic processing. Given that ion transport often dictates switching speed, regulation of intercalation kinetics has emerged as a critical pathway for enabling next generation, high-speed, energy-efficient synaptic devices.[21]

Ion intercalation is known to induce pronounced structural and electronic modifications in layered and framework materials.[22] For example, multilayer 2*H*−MoS_2, with its large interlayer spacing of 0.62 nm, offers abundant storage sites and rapid diffusion channels for Li^+ ions, enabling reversible conductance modulation under an applied field.[22−24] Porous electrochemical solids represent another particularly attractive class of materials in this context. In particular, metal−organic frameworks and coordination polymers offer exceptional opportunities because their composition, redox chemistry, and host−guest interactions can be tuned synthetically, allowing the electrochemical window of the lattice, and thus the ion-migration-driven memristive response, to be engineered by design.[25−30] However, many such systems still suffer from limited cycling stability and spatially inhomogeneous ion migration, which hinder reproducible switching and long-term device operation.

In this context, Prussian blue (PB) and its analogues (PBAs), among the earliest known coordination polymers, have emerged as especially appealing candidates for iontronic switching applications. Their attractiveness stems from a rigid open framework with well-defined cavities for alkali-ion insertion and stabilization, combined with a redox-active transition-metal lattice that can sustain both filamentary and ion-migration-driven memristive switching over hundreds to thousands of cycles without significant structural fatigue.[31,32] PBAs can be described by the general formula:

$$AQ\left[M(CN)_6\right] \quad (1)$$

where (A = Li, K, Na; Q = Fe, Co, Ni, Mn, Cu; and M = Fe, Mn, Co, etc.), in which alkali-metal ions occupy spacious cubic cavities within a rigid Fe−C≡N−Fe network.[33] In these materials, alkali-metal ions occupy spacious cubic cavities within a face-centered cubic cyanometallate network composed of transition-metal octahedra linked by cyanide ligands. This intrinsic architecture gives rise to three-dimensional ion-diffusion pathways, strong coupling between ion distribution and Fe^{2+}/Fe^{3+} redox states, and electronically tunable mixed-valence transport.[34] Consequently, PBAs have recently gained attention as versatile candidates for ion-intercalation memristors and neuromorphic devices.

Despite this promise, mechanistic insight into the local switching processes of PB/PBA-based memristors remains limited. In particular, few studies have probed memristive behavior with sufficient spatial resolution to directly resolve the ionic dynamics that underlie it. As a consequence, the relationship between local ion migration, redox redistribution, and resistive switching remains poorly understood, hindering the rational design of PBA-based iontronic devices.

Here, we address this challenge by locally investigating the memristive response of two representative end members of the PBA family, Prussian white (PW) and Prussian blue (PB), which differ primarily in their K^+ content and Fe oxidation-state distribution.[35,39] This chemically defined contrast provides an ideal platform for elucidating how alkali-ion content governs nanoscale resistive switching. By combining conductive atomic force microscopy (C-AFM), finite-element simulations, and in situ Raman spectroscopy, we correlate the local memristive response of electrodeposited PW and PB thin films with their intrinsic K^+ concentration and redox chemistry. We show that these differences directly determine the switching polarity, with both PW and PB exhibiting URS at opposite bias polarities, and demonstrate that the resistive switching is governed by a nanoscale, electrically confined ion−electron coupling mechanism involving K-ion redistribution and redox-modulated small-polaron transport beneath the probe.[40]

Beyond clarifying the local switching mechanism, our results establish electrodeposited MOF PBAs as a chemically tunable and scalable materials platform for low-dimensional memristive devices and neuromorphic computing. By directly correlating ion migration, redox transformations, and electronic conduction at the nanoscale, this work addresses one of the central knowledge gaps highlighted by Aluru et al.[41] for neuromorphic ionic computing: understanding and controlling coupled ionic−-electronic transport in functional materials. These findings further demonstrate the potential of PBAs as a model platform for ion-intercalation-based information processing.

RESULTS

Figure 1 presents Fe and K elemental maps obtained by energy-dispersive X-ray spectroscopy (EDS), demonstrating the precise compositional control achievable in electrodeposited MOF PBA thin films. Films deposited between 0.1 and 0.25 V correspond to the Prussian White (PW), whereas deposition potentials above 0.28 V produce Prussian Blue (PB). The EDS analysis reveals a systematic decrease in K content with increasing deposition potential, reflecting the transition from the reduced, K-rich PW phase to the more oxidized PB phase. This behavior is consistent with the different Fe valence configurations of the two phases, where the reduced PW framework requires a larger concentration of interstitial K^+ ions for charge compensation. To better visualize how this balance occurs, the corresponding chemical formulas are shown in Figure 1.

The ability to tune the interstitial K^+ concentration through electrodeposition provides direct control over the redox state, charge distribution, and ionic environment of the PBA framework, all of which are expected to influence charge transport. To investigate these effects, two compositions well separated from the PW−PB transition region were selected: PW deposited at 0.1 *V*, containing approximately 50% K^+, and PB deposited at 0.3 V, containing approximately 30% K^+. The two phases are also easy distinguished by their characteristic coloration, as shown in Figure 1. Additional morphological information is provided in Figures S1 and S2.

C-AFM measurements were performed to probe the nanoscale resistive switching behavior of the two PBAs phases (Figure 2a,d). Current maps acquired over 1 × 1 μm^2 areas at a bias of 1 V (Figure 2b,e) reveal clear conductance differences between the two phases. This contrast in conductivity is directly linked to the conduction mechanism of these coordination

https://doi.org/10.1021/acsaelm.6c00766
ACS Appl. Electron. Mater. XXXX, XXX, XXX−XXX

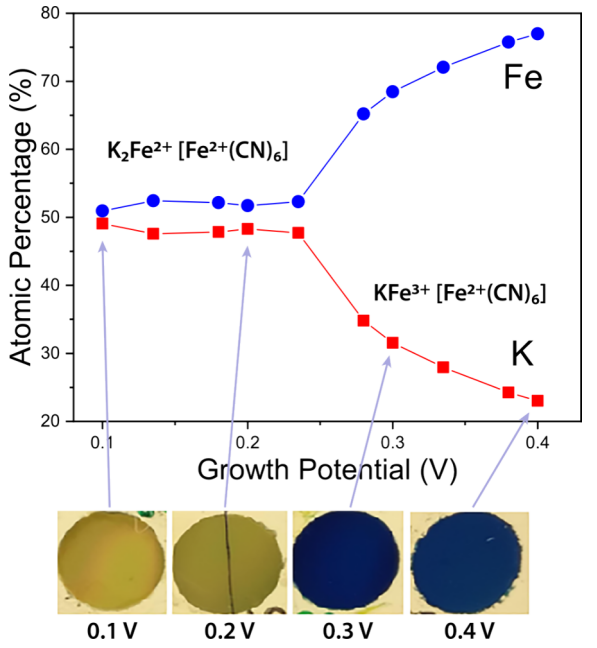

Figure 1. Atomic percentages derived from energy-dispersive X-ray spectroscopy (EDS) elemental maps of Fe and K illustrating controlled evolution of composition from PW to PB. As the electrodeposition potential increases, the materials exhibit a clear transition from K-rich PW to progressively K-deficient PB.

materials, which is governed by polaron-assisted transport arising from mixed Fe^{2+}/Fe^{3+} metal centers.[42] In PW, the reduced fraction of Fe^{3+}, at the expense of an increased Fe^{2+} content, suppresses this mixed valence pathway, resulting in a lower overall conductivity. This behavior is consistent with the expansion of the electronic band gap theoretically predicted in PW.[43] The blue crosses overlaid on the current maps in Figure 2b,e mark the precise nanoscale locations at which individual $I-V$ measurements were acquired using the C-AFM probe. These marked points correspond directly to the $I-V$ curves presented in Figure 2c,f, where the electrical response of each selected site is shown in detail. The measurements were carried out using a positive-bias sweep from 0 to 10 V at a constant ramp rate of 0.1 V/s (same protocol applied uniformly across all experiments), this controlled sweep condition enables consistent probing of the switching polarity and reliable quantification of the resistive-state modulation. The resulting $I-V$ characteristics exhibit well-defined SET and RESET transitions, clearly revealing the transition between the low-resistance (LRS) and high-resistance (HRS) states for both PW and PB. Additional nanoscale mapping details are provided in Figures S3 and S4, including C-AFM topography maps acquired prior to $I-V$ measurements at varying point spacings.

From the perspective of the existing literature, the conductivity of PB is primarily governed by polaron hopping. The memristive behavior of PB films can be rationalized in a manner analogous to that of light-emitting electrochemical cells.[44] PB

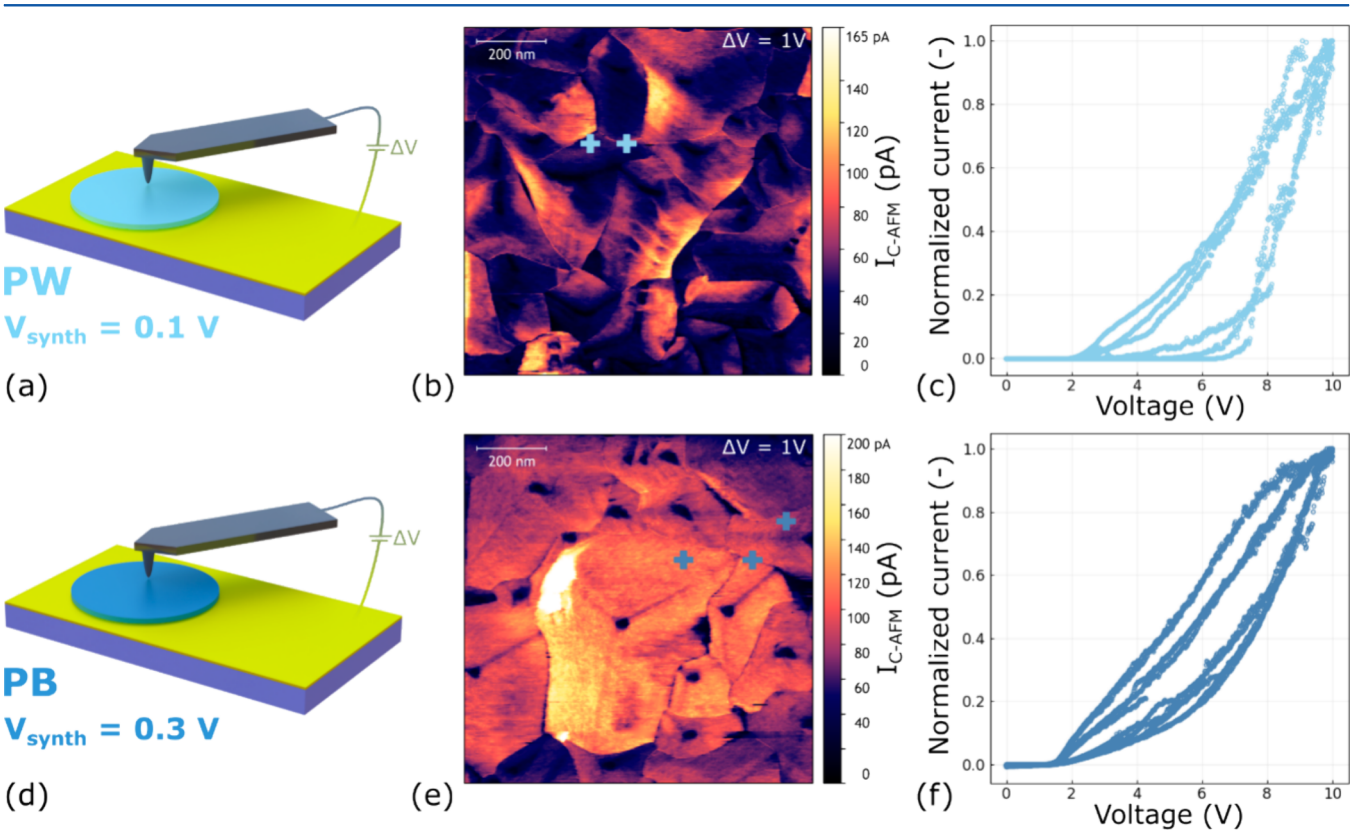

Figure 2. C-AFM measurements on PBA samples. (a, d) Illustrations of the measurement configuration on Prussian white (PW) and Prussian blue (PB) samples, respectively. (b) Current map obtained with a 1 × 1 μm C-AFM scan on (b) PW and (e) PB with a 1 V bias voltage. Multiple $I-V$ sweeps (c) PW and (f) PB samples acquired at different locations of the C-AFM scans, shown by the markers in (b) and (e).

https://doi.org/10.1021/acsaelm.6c00766
ACS Appl. Electron. Mater. XXXX, XXX, XXX−XXX

contains mobile counterions that enable reversible oxidation and reduction of the Fe centers, as K^+ ions can migrate through the framework cavities to locally compensate charge. Under positive tip bias, electrons are extracted from the material and collected at the tip, while the substrate supplies electrons, promoting local oxidation processes associated with $Fe^{2+} \rightarrow Fe^{3+}$ conversion. Above a characteristic threshold voltage (approximately 2−4 V for PB and around 7 V for PW, Figure 2), the *I*−*V* characteristics exhibit rectifying behavior. Below threshold, current is injection-limited (contact barrier− limited), leading to low residual conduction. We extract the exact mechanism via the data treatment of the current vs voltage data. Once the threshold is exceeded, efficient electron and/or hole injection occurs, leading to an exponential increase in current. In this context, this injection of charge carriers also alters the oxidation state of the Fe centers, thereby generating the memristive response, which persists after the applied bias is removed.

To obtain a more precise evaluation of the RS behavior in the two PBA phases, local *I*−*V* scans by C-AFM were performed in a hysteresis range of −10 to + 10 V, with a scan rate of 1 V/s (Figure 3). The *I*−*V* characteristics of the PW film (Figure 3a) exhibit clear URS, where the SET and RESET transitions occur under the same voltage polarity. This nanoscale URS response is fully consistent with previous macroscopic measurements obtained using conventional upper and lower electrode configurations, as reported for PW-based devices in the literature,[35−37,45,46] with a predominance of the current response in the negative polarity. In contrast, the PB film exhibits URS behavior (Figure 3b), with a smaller electrical response and a predominance of the current response now in the positive polarity. C-AFM measurements demonstrate that both PBA phases, retain intrinsic nanoscale resistive switching, with both systems exhibiting URS. In each case, the switching is confined to a single bias polarity, although the preferred polarity is opposite for PW and PB. This polarity-dependent behavior is consistent with distinct redox-driven conduction mechanisms in the two phases. Upon closer examination, the memristive response in PW is attributed to oxidation-induced conductivity enhancement, whereas in PB it is associated with reduction. This interpretation is consistent with the redox states of the materials: PW, as the most reduced phase, has limited capacity for further reduction, such that slight oxidation increases charge carrier density and activates polaron hopping pathways. In contrast, PB, which is intrinsically mixed-valent and may deviate from ideal stoichiometry toward a partially over-oxidized state, exhibits enhanced conductivity after slight reduction. In both cases, the switching behavior can, therefore, be rationalized in terms of redox-modulated small-polaron transport within the PBA framework.

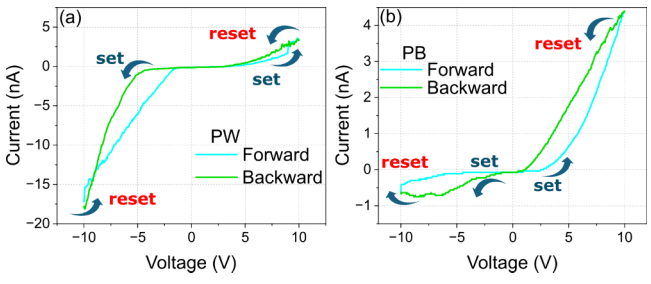

Figure 3. Current−voltage characteristics measured by C-C-AFM. (a) PW film exhibiting unidirectional resistive switching at a single bias polarity. (b) PB film also showing URS, with switching occurring at the opposite polarity to PW.

To assess the dynamical limits of the RS mechanism, voltage-ramp measurements were performed at a fixed location, and varying the sweep rate. Although C-AFM offers high spatial resolution, it is not suitable for endurance cycling. Repeated measurements can induce tip drift, contact degradation, and local surface damage, while the measured current is also sensitive to time-dependent effects and ambient conditions such as relative humidity.[47,48] Consequently, changes observed during prolonged cycling may reflect measurement artifacts rather than intrinsic material behavior. Therefore, to probe the intrinsic RS behavior of PW and PB surfaces, 10 consecutive C-AFM voltage sweeps were performed from 0 to +10 V at the same spatial location with a scan rate of 0.1 V/s. This voltage range was selected to avoid polarity-induced conditioning effects observed in full bipolar sweeps (−10 to +10 V), which introduce history-dependent variability in the current response, thereby ensuring reproducible measurements and direct comparison between PW and PB under identical conditions. The corresponding results are shown in Figures S5 and S6 for PW and PB, respectively.

This measurement strategy is consistent with the methodology established by M. Lanza and co-authors,[48] who demonstrated that C-AFM is an effective approach for vali dating RS in ultrashort metal−insulator−metal (MIM) cells by emulating nanoscale device geometries. In this work, the authors emphasized that C-AFM is well suited for spatially resolved RS studies. Following these guidelines, our approach prioritizes spatial mapping and statistical assessment of RS behavior over extended cycling at individual sites, ensuring reliable nanoscale characterization. The *I*−*V* characteristics consistently exhibit the key features of resistive switching, confirming that the effect is reliably captured at the nanoscale. Although cycle-to-cycle variability is observed, consistent with nanoscale measurement conditions. Such variability is expected given the inherent sensitivity of C-AFM measurements to tip−sample contact stability, local surface modifications, and environmental factors as was already mentioned above. Importantly, the persistence of the switching response across repeated sweeps demonstrates the robustness of the RS mechanism in both materials.

After characterizing the switching behavior at a fixed location in the sample, we examined the RS effect for different voltage sweep rates. Measurements were performed at ten distinct locations in each sample, separated by 500 nm, to assess spatial variability. For the PW films, voltage ramps were applied over a range of sweep rates (0.2, 0.5, 1.0 ,2.0, 10, 50, 100, and 200 V/s), results shown in Figure S7. Resistive switching behavior persisted up to 200 V/s, although with reduced current levels. For the PB films, we observed a similar trend, but with a lower kinetic threshold: resistive switching persisted only up to 50 V/s, results shown in Figure S8.

After establishing that the RS effect is reproducible in repeated measurements and remains observable over a wide range of voltage sweep rates, we investigated its spatial distribution through systematic *I*−*V* mapping. Predefined measurement grids, with controlled scan areas and point spacing, were programmed using the C-AFM instrument control software, enabling precise electrical characterization at the nanoscale. The resulting maps for PW and PB are shown in Figures 4 and 5, respectively, with crosses indicating the locations of each individual *I*−*V* measurement.

https://doi.org/10.1021/acsaelm.6c00766
ACS Appl. Electron. Mater. XXXX, XXX, XXX−XXX

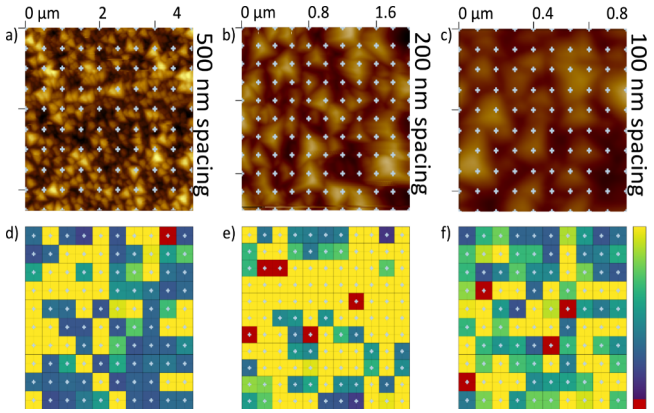

Figure 4. C-AFM map. (a–c) Topography maps of the PW film acquired over areas of 5 × 5 μm^2, 2.5 × 2.5 μm^2, and 1 × 1 μm^2, respectively. The markers (crosses) indicate the precise locations at which *I*–*V* curves were recorded, with inter-point spacings of 500 nm, 200 nm, and 100 nm, respectively. (d–f) Color-coded heat maps of the HRS/LRS current ratio extracted from C-AFM *I*–*V* measurements on the PW film, corresponding to the measurement grids shown in (a–c). The maps were obtained for inter-point spacings of 500 nm (d), 200 nm (e), and 100 nm (f). Nonfunctional cells, exhibiting a very low or near-zero HRS/LRS ratio, are shown in red, whereas functional switching sites appear from blue to green. PW exhibits high RS yields of 99%, 96%, and 96% for the 500, 200, and 100 nm grids, respectively.

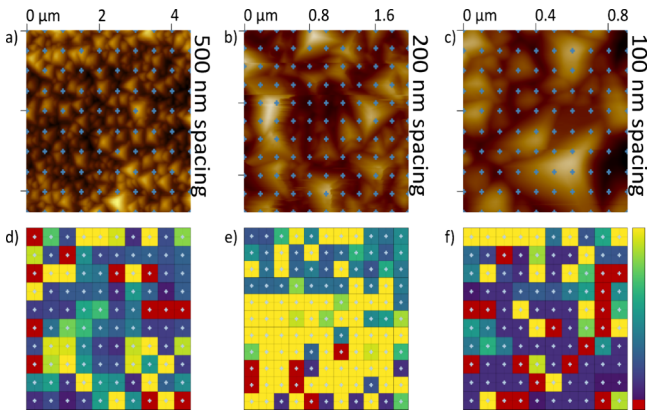

Figure 5. C-AFM map. (a–c) Topography maps of the PB film acquired over areas of 5 × 5 μm^2, 2.5 × 2.5 μm^2, and 1 × 1 μm^2, respectively. The markers (crosses) indicate the precise locations at which *I*–*V*curves were recorded, with inter-point spacings of 500, 200, and 100 nm, respectively. (d–f) Color-coded heat maps of the HRS/LRS current ratio extracted from C-AFM *I*–*V* measurements on the PB film, corresponding to the measurement grids shown in (a–c). The maps were obtained for inter-point spacings of 500 (d), 200 (e), and 100 nm (f). Nonfunctional cells, exhibiting a very low or near-zero HRS/LRS ratio, are shown in red, whereas functional switching sites appear from blue to green. PB exhibits RS yields of 88%, 95%, and 83% for the 500, 200, and 100 nm grids, respectively.

Three mapping configurations were employed for the films. First, a 5 × 5 μm^2 area was probed using a 10 × 10 grid (100 points) with a lateral spacing of 500 nm between adjacent points (PW in Figure 4a and PB in Figure 5a). The mapping area was then reduced to 2.5 × 2.5 μm^2, with the point spacing decreased to 200 nm, resulting in an 11 × 11 array comprising 121 measurement points (PW in Figure 4b and PB in Figure 5b). Finally, high-resolution mapping was performed over a 1 × 1 μm^2 area using a 10 × 10 grid with a spacing of 100 nm (PW in Figure 4c and PB in Figure 5c), enabling detailed nanoscale assessment of local RS effect.

At each measurement site, two consecutive *I*–*V* sweeps from 0 to 10 V were recorded to probe the local RS response while limiting cumulative electrical stress on the active layer, all the raw data is available on the GitHub link in the methods section. Although C-AFM is a powerful technique for investigating RS phenomena with nanometer-scale resolution, repeated electrical cycling at a single location can lead to irreversible local modifications, including Joule heating, filament overgrowth, or mechanical degradation of the tip–sample contact. To avoid such artifacts and to preserve the intrinsic switching behaviour, each mapping configuration was therefore performed on a new, nonoverlapping region of the film surface.

After completing all the *I*–*V* measurements, each curve was analyzed individually to determine whether resistive switching is showing. For every measurement site, the HRS/LRS current ratio was calculated and used as a quantitative metric of switching performance. Points with an HRS/LRS ratio ≥ 1.5 were classified as functional RS cells, whereas lower ratios were considered nonfunctional. The resulting HRS/LRS values were represented as color-coded heat maps, providing a direct visualization of both the spatial distribution and intensity of the RS behavior across the C-AFM nanoscale arrays.

In the color scale, cells classified as nonfunctional are represented in red with a very low or nonexistent HRS/LRS ratio, while cells in the blue to green range correspond to moderate, but distinguishable, HRS/LRS ratios. High-performance switching sites, characterized by large resistance contrasts, appear in the green to yellow range, indicating greater robustness of the resistive switching. As shown in Figure 4d for PW and Figure 5d for PB, the 500 nm-spaced arrays reveal a high density of functional cells, with PW exhibiting RS at 99% of the measured points and PB at 88%. When the interpoint, spacing was reduced to 200 nm, the fraction of active sites remained high, reaching 96% for PW and 95% for PB. At the highest spatial resolution of 100 nm, PW maintained a consistently high yield of 96%, whereas PB showed RS at 83% of the probed locations. The color map analysis provides a clear visualization of both the spatial uniformity and the robustness of the resistive switching response. The PW film exhibits a more homogeneous distribution of active switching sites and a larger fraction of locations with high HRS/LRS ratios, represented by the yellow regions in the map. This indicates not only a higher yield of functional cells but also more stable and pronounced resistance contrast across the probed area.

To obtain a deeper understanding of how nanoscale memristive responses interact within the mapped arrays and to obtain a more detailed view of the switching mechanism itself, finite-element simulations were performed to model the tip-induced electric field during C-AFM measurements. While such simulations have traditionally been used to interpret C-AFM responses in isotropic dielectric or semiconductor materials,[49−51] they have not been applied to PBAs. Here, the model was established considering 25 nm tip radius and micrometer-scale equipotential layers representing the lateral extent of the PW and PB films. The resulting potential distributions (Figure 6 left-PW, right-PB) show that the electric field is highly localized: the potential

https://doi.org/10.1021/acsaelm.6c00766
ACS Appl. Electron. Mater. XXXX, XXX, XXX–XXX

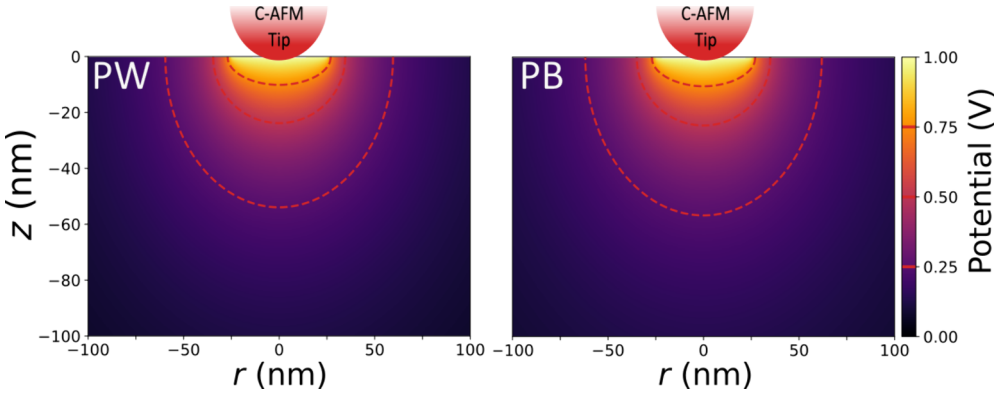

Figure 6. Simulated electrostatic potential distribution below the conductive C-AFM tip for (left) Prussian white and (right) Prussian blue, illustrating the strong nanoscale confinement of the electric field within the PBA framework.

penetrates effectively only up to ∼60 nm both laterally and vertically from the tip−sample junction. This short penetration depth is significantly smaller than the smallest spacing used in our experimental memristive arrays (100 nm), demonstrating that neighboring points do not influence each other. Each memristive site, therefore, behaves as an electrically independent nanoscale cell, and measurements performed on adjacent points do not introduce crosstalk or interference.

The simulations also clarify the underlying physical origin of this strong localization. Because PBAs contain interstitial K^+ ions, their interaction with the applied electric field is important: K^+ experiences a force along the field direction and migrates from regions of lower to higher electric potential. This field-driven redistribution contributes to short-range ionic shielding, further confining the electric field and modifying the local conductivity pathways only within the immediate vicinity of the C-AFM tip. Consequently, the tip−sample contact behaves as an effectively isotropic region, because the electric field is confined to a ∼60 nm volume where the cubic Fe−C≡N−Fe framework, together with shortrange K^+ ionic shielding, generates a locally homogeneous electrostatic environment. This short-range shielding arises from the fact that interstitial K^+ ions can undergo only limited displacements within their coordination cavities, enabling them to partially compensate for the applied field but only over nanometric distances. The resulting confinement of the electric perturbation prevents lateral field propagation, ensuring that each memristive site in the array operates independently, without interference even at the smallest spacing of 100 nm. This local isotropy is consistent with the intrinsic tridimensional connectivity of the PBA structure. Furthermore, analysis of experimental measurements confirms that there is no dependence between the surface thickness variations of the PBA layer and the electrical response of the material (see Supporting Information Figure S9). This demonstrates that the switching process is a local process that takes place in the region of penetration of the electric field.

Figure 7 shows how the electric field generated by the CAFM tip modifies the PW, providing chemical spectroscopic evidence of the switching mechanism being a combination of oxidation/reduction and K-ion intercalation. The Raman spectroscopy was performed directly at the sites previously addressed by C-AFM, establishing a one-to-one correlation between the local electrical excitation and the corresponding chemical change. The in situ Raman measurements (532 nm, 0.4 mW) probe a substantial fraction of the active film thickness and reveal reversible PW ↔ PB spectral transitions at electrically stimulated locations. These changes provide direct spectroscopic evidence of Fe^{2+}/Fe^{3+} redox transformations coupled to K^+ redistribution within the PBA framework. The optical image shows the 5 × 5 μm^2 region previously examined by C-AFM (Figure 7a). The arrow indicates the position and direction of the scan in which the 50 consecutive spectra were acquired, allowing high-resolution monitoring of the vibrational changes induced by the electric field.

The Raman spectra reveal clear modifications in the PW film when an external voltage sweeps. In the as-prepared state, the film exhibits three principal CN stretching contributions: bands near ∼2080 and ∼2120 cm^{-1}, attributed to Fe^{2+}−CN−Fe^{2+} linkages and/or uncoordinated $Fe(CN)_6^4$ units, together with a higher-frequency component at ∼2155 − 2160 cm^{-1} associated with Fe^{2+}−CN−Fe^{3+} linkages. These assignments are consistent with reported bulk PW references, which also contain PB-like Fe^{2+}−CN−Fe^{3+} species (presented in Figure S10). Thus, even in the nominally reduced PW state, the film contains a mixed-valence population rather than a purely Fe^{2+}−CN−Fe^{2+} configuration. Upon voltage application, the intensity of the Fe^{2+}−CN−Fe^{3+} band at ∼2156 cm^{-1} increases at the expense of the lower frequency modes. This redistribution of spectral weight indicates electrically induced oxidation of Fe^{2+} toward Fe^{3+}, enhancing PB-like linkages within the PBA lattice.

The spatial distribution of this redox modulation is visualized in Figure 7b through a 2D confocal Raman spectroscopy map centered on the ∼2156 cm^{-1} band. Brighter regions correspond to areas with a higher fraction of Fe^{2+}−CN−Fe^{3+} units, whereas darker regions reflect more reduced environments enriched in Fe^{2+}−CN−Fe^{2+} uncoordinated species. The contrast demonstrates a heterogeneous mixed-valence landscape within the film that evolves under electrical polarization.

To directly compare regions that did and did not experience voltage stress, Figure 7c shows spectra acquired sequentially along the line scan in Figure 7a. The first spectrum (cyan) exhibits the mixed PW-like signature with contributions from Fe^{2+}−CN−Fe^{2+} uncoordinated species and a weaker Fe^{2+}−CN−Fe^{3+} shoulder. At the electrically biased position (blue), the ∼2156 cm^{-1} band dominates, reflecting oxidation and increased PB-like character. A subsequent spectrum

https://doi.org/10.1021/acsaelm.6c00766
ACS Appl. Electron. Mater. XXXX, XXX, XXX−XXX

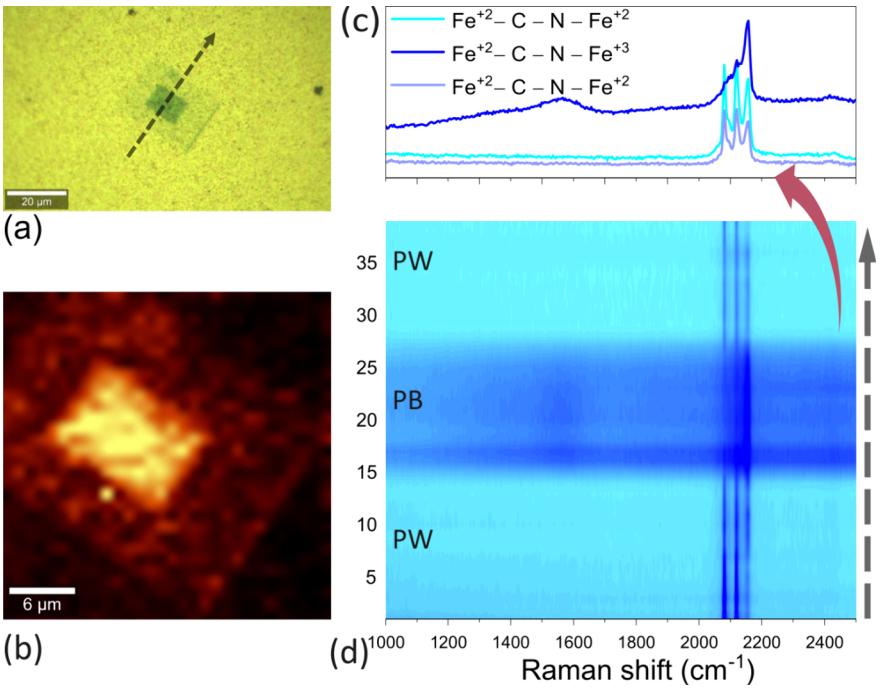

Figure 7. Influence of the C-AFM tip on the redox state of PW. (a) Optical micrograph of the 5×5 μm^2 region in which the C-AFM experiment was performed 50 spots full Raman spectrum showing the transition from PW to PB and back to PW. The arow indicate direction the direction in which the Raman mapping was performed. (b) 2D confocal Raman intensity map acquired around the ∼2156 cm^{-1}. (c) Raman spectra highlighting the characteristic vibrational modes of PW (2080, 2118, and 2156 cm^{-1}, shown in cyan/malibu) and PB (2122 and 2155 cm^{-1}, shown in blue). (d) 2D Raman contour map illustrating the temporal evolution of the Raman signal from 1000 to 2500 wavelength, and the distinct transition from PW and PB regions. The arow indicate Raman mapping direction.

recorded further along the scan (violet) resembles the initial state, indicating that the redox modulation is reversible and that the film recovers a similar mixed-valence distribution after removal of the voltage.

Figure 7d shows a 2D Raman contour map that captures the spatial evolution of the vibrational response, clearly showing the PW → PB → PW transition. The confined electric field beneath the C-AFM tip induces localized, reversible intercala tion and redistribution of interstitial K^+ ions, which modulates the Fe^{2+}/Fe^{3+} balance within the Fe−CN−Fe network while preserving the structural integrity of the PBA lattice. The close correspondence between the field-induced Raman evolution and established vibrational fingerprints of PBAs with varying K^+ content and redox state provides strong evidence that nanoscale resistive switching in PW arises from localized K^+ migration coupled to Fe-center redox reconfiguration, rather than from irreversible chemical or structural changes or damages.

■ DISCUSSION

The results presented here indicate that resistive switching in electrodeposited MOFs PBAs is governed by a localized ion−electron coupling mechanism in which short-range K^+ redistribution is directly linked to changes in the Fe^{2+}/Fe^{3+} ratio within the Fe−C≡N−Fe framework. Unlike conventional oxide-based resistive switching systems, where conductivity is often controlled by the stochastic formation and rupture of conductive filaments, the switching process in PBAs emerges from a reversible electrochemical interaction between ionic motion and electronic transport. Because charge transport in PBAs occurs through intervalence electron hopping between adjacent Fe^{2+} and Fe^{3+} centers, even subtle modifications of the local redox environment can strongly influence conductivity. The distinct switching behavior observed for PW and PB further highlights the importance of alkali-ion concentration, suggesting that ionic occupancy plays a central role in defining the kinetics of the switching process.

The finite-element simulations provide additional insight into the spatial nature of this mechanism. The calculated confinement of the electric field to a region extending only 60 nm in volume beneath the C-AFM tip suggests that the electrochemical processes responsible for switching are highly localized. Such confinement is particularly relevant because it implies that ionic redistribution remains restricted to a small active volume, limiting electrical interaction between neighboring regions. This interpretation is consistent with the high switching yields observed experimentally even at the smallest pitch investigated (100 nm), supporting the possibility of dense integration without significant crosstalk between adjacent memristive elements.

Another noteworthy aspect of the present study is the unusually fast switching dynamics observed in these intercalation-based systems. Ion-intercalation mechanisms are commonly associated with relatively slow processes due to the time required for ionic migration and redox equilibration.[52−58] However, PW maintains stable switching behavior at sweep rates up to 200 V/s, while PB remains functional up to 50 V/s. These values are substantially higher than those typically reported for Li^+- and Na^+-based intercalation memristors.[36,59,60] This behavior suggests that the open three-dimensional architecture

https://doi.org/10.1021/acsaelm.6c00766
ACS Appl. Electron. Mater. XXXX, XXX, XXX−XXX

of PBAs provides efficient ion-transport pathways capable of supporting rapid electrochemical responses. The superior performance of PW compared with PB is likely related to its larger concentration of mobile K^+ ions, which facilitates faster local charge compensation and accelerates redox equilibration under an applied electric field.

These observations also contribute to the growing body of evidence that ion intercalation can serve as an alternative switching mechanism to the filamentary processes traditionally associated with memristive devices. Recent work by He et al. demonstrated that resistive switching in PBA-based devices originates from reversible Na^+ insertion and extraction rather than metallic filament formation.[61] The present results extend this concept by showing that K^+ intercalation can produce a similar effect at the nanoscale while sustaining substantially faster switching dynamics. More broadly, these findings highlight the potential of PBAs as model systems for investigating the interplay between ionic transport, redox chemistry, and electronic conduction in memristive materials.

The Raman measurements provide an important chemical perspective on this mechanism. The reversible evolution between PW-like and PB-like vibrational signatures demonstrates that the electrical stimulus induces a dynamic reorganization of the Fe^{2+}/Fe^{3+} population rather than irreversible structural modification of the framework. Because the oxidation state of Fe in PBAs is intrinsically coupled to the distribution of interstitial K^+ ions, these spectroscopic changes provide strong evidence that the electrical response is governed by reversible electrochemical processes. Furthermore, the spatial variations observed in the Raman maps reveal that local differences in redox state and alkali-ion distribution persist throughout the films, which may contribute to the variability commonly observed in nanoscale switching measurements.

Electrodeposited PBA MOFs represent a fundamentally different class of memristive materials, in which resistive commutation is governed by reversible ion intercalation coupled to redox chemistry within an ordered crystalline structure. The exceptional compositional versatility of the PBA family offers a unique opportunity to systematically adjust commutation characteristics by selecting alkali ions, transition metal centers, vacancy concentrations, and redox states, thus opening a broad path with new ion-intercalation memristive materials.

■ CONCLUSIONS

In this work, we demonstrate that K-ion intercalation is the fundamental mechanism governing resistive switching in electrodeposited MOF PBA thin films and that this process can be directly resolved at the nanoscale. Through conductive AFM measurements, finite-element simulations, and in situ Raman spectroscopy, we establish that reversible K^+ redistribution drives Fe^{2+}/Fe^{3+} redox transformations within the Fe−C≡N−Fe framework, modulating intervalence electron hopping and producing reversible conductance changes without evidence of permanent structural modification.

The switching behavior is strongly influenced by the alkali-ion content and redox state of the framework. The higher K^+ concentration in PW promotes faster ionic redistribution and redox equilibration, enabling switching at sweep rates up to 200 V s^{-1}, whereas PB remains operational up to 50 V s^{-1}. These results demonstrate that ionic occupancy is not merely a compositional parameter, but a key design variable governing the speed and functionality of intercalation-driven memristive devices.

More broadly, this work establishes PBAs as a fundamentally different class of memristive materials in which information is encoded through reversible ion intercalation and redox chemistry within an ordered crystalline framework. The exceptional compositional versatility of the PBA family, combined with nanoscale switching confinement, fast ionic dynamics, and single-step room-temperature electrodeposition from earth-abundant precursors, provides a unique platform for engineering future memory and neuromorphic devices.

Beyond clarifying the local switching mechanism, these findings address one of the central knowledge gaps identified for neuromorphic ionic computing: understanding and controlling coupled ionic−electronic transport in functional materials. By translating a well-established battery intercalation process into a nanoscale information-storage mechanism, this work positions electrodeposited MOF-PBAs as a new class of fast ion-intercalation memristive material and highlights their potential for next-generation memory and neuromorphic computing technologies.

■ METHODS

PBAs Synthesis

The dielectric layer, consisting of a Prussian blue analog (PBA) thin film, was deposited at room temperature by electrochemical deposition in potentiostatic mode using an electrochemical workstation (Ivium CompactStat, Eind hoven, Netherlands). Electrodeposition was carried out in a conventional three-electrode configuration controlled by a potentiostat. The working electrode (WE) was an Au/Cr/Si substrate, fabricated by electron-beam evaporation of a 5 nm chromium adhesion layer followed by a 50 nm gold layer onto a (100)-oriented silicon wafer (1 × 1 cm^2), under a base pressure of 10−5 Pa. Film growth was confined to a circular area of 0.5 cm2 defined by an adhesive tape mask applied during sample preparation. A platinum foil was used as the counter electrode (CE), and a saturated calomel electrode (SCE) served as the reference electrode (RE). The electrolyte consisted of an aqueous solution containing 1.0 M KCl, 5.0 mM HCl, 0.5 mM FeCl3, and 0.5 mM K3Fe(CN)6 (ACS grade, > 99%, Sigma−Aldrich, Darmstadt, Germany), prepared in 100 mL of deionized water with the pH adjusted to 2. Film deposition was achieved by applying a constant potential versus the SCE, enabling precise control of the electrodeposition process by limiting the total transferred charge. For all samples, a total charge of 10 mC was deposited, yielding estimated film thicknesses of approximately 300 nm for Prussian White (PW) films deposited at 0.1 V and 500 nm for Prussian Blue (PB) films deposited at 0.3 V. All depositions were performed at 25 °C. Notably, no postdeposition thermal or chemical treatments were required, which simplifies the fabrication process and reduces overall processing complexity. Additional details on the electrochemical setup and deposition protocol can be found in ref 38.

Morphology and Composition

Morphological and compositional properties were analyzed by field emission scanning electron microscopy (FEG-SEM, TESCAN CLARA, Brno, Czech Republic) equipped with an energy-dispersive X-ray (EDX) detector (Ultim Max 65 SDD, Oxford Instruments, Wiesbaden, Germany) at 20 keV and a Raman system (Witec RISE, Ulm, Germany). Raman measure ments were performed with a 532 nm laser at 0.4 mW.

C-AFM measurements

Conductive Atomic Force Microscopy measurements are conducted on a Bruker Icon Dimension equipped with a CAFM module. The

https://doi.org/10.1021/acsaelm.6c00766
ACS Appl. Electron. Mater. XXXX, XXX, XXX−XXX

measurements are obtained with SCM-PITV2 probes from Bruker. Those have a Pt/Ir metallic coating and a 25-nm radius, an elastic constant of 3 nm^{-1} and a resonance frequency of 75 kHz. A thermal tune calibration of the tip is done before the measurements to update the elastic constant value. During the C-AFM scans, the deflection setpoint is kept between 50 and 70 nm and adjusted to optimize the signal quality and stability. *I*−*V* curves are then acquired at specific locations with a volage sweep between 0 and 10 V on every sample while keeping the same parameters as for the scan. The data treatment was carried out using Gwyddion and Nanoscope softwares, as well as the pySPM library [Scholder, O. scholi/pyspm: pyspm v0.2.16 (version v0.2.16). https://doi.org/10.5281/zenodo.998575].

Simulation

Finite-element simulations were carried out in COMSOL Multiphysics using an axisymmetric geometry. The Solid Mechanics and Electric Currents modules were employed sequentially to first determine the mechanical deformation induced by the CAFM tip and subsequently compute the resulting electric potential and current distribution. During the mechanical step, a normal load of 180 nN, corresponding to the experimental CAFM conditions was applied to the tip. The tip was modeled as a rigid indenter penetrating a linear-elastic, isotropic medium representing the sample. The resulting indentation profile and stress distribution within the material were obtained from this step and used as input for electrical simulation. For the electrical step, a bias of 1 V was applied to the tip while the bottom electrode was grounded. The lateral boundaries of the sample were set as electrically insulating so that no current could exit through the sidewalls. The electric potential distribution and total current through the bottom electrode were then computed assuming an isotropic conductivity. Two sample thicknesses were considered: 500 nm for PB and 300 nm for PW. The lateral size of the computational domain and the mesh densities were chosen based on convergence analyses performed on (i) the indentation depth, (ii) the total transmitted current, (iii) the potential evaluated 3 nm below the surface, and (iv) the residual current leaking through the lateral boundaries. These criteria ensured that both the mechanical deformation and the electrical response were independent of the domain size and mesh discretization.

Data Analysis and Plots

All figures presented in this work were generated using a custom method, Python-based plotting framework that we developed for this study. To ensure full transparency and reproducibility, the complete repository including the raw data, processing scripts, and figure-generation code, is openly available on GitHub (https://github.com/AlTemporao/k-ionintercalation-memristors-in-pbas). No numerical simulations or model fitting were performed; all results reflect direct analysis of the experimental data. Based on the roughness measured by the AFM, we correlated the thickness variations of the PW (and PB) layers at different locations with the *I*−*V* curves measured at those locations. Then, using in-house Python scripts, we plotted those IV curves at the LRS with a color scale to identify thickness differences between points. We used the LRS as a reference state for this figure because if the RS process depends on the thickness of the switching layer, a clear correlation between the current and the thickness variations is expected.

■ ASSOCIATED CONTENT

Data Availability Statement

The data that supports the findings of this study are available in the Supporting Information of this article and at the GitHub.

Supporting Information

The Supporting Information is available free of charge at https://pubs.acs.org/doi/10.1021/acsaelm.6c00766.

Morphological characterization by SEM; additional conductive AFM (C-AFM) topography and current mapping; repeated C-AFM *I*−*V* measurements; voltage sweep rate-dependent resistive switching measurements; AFM variation analysis; reference Raman spectra of bulk Prussian White and Prussian Blue (DOCX)

■ AUTHOR INFORMATION

Corresponding Authors

Lindiomar Borges de Avila Junior – *Institute of Condensed Matter and Nanosciences (ICMN), Université catholique de Louvain (UCLouvain), Louvain-la-Neuve 1348, Belgium;* orcid.org/0000-0001-9039-2498; Email: lindiomar.borges@uclouvain.be

Flavio Abreu Araujo – *Institute of Condensed Matter and Nanosciences (ICMN), Université catholique de Louvain (UCLouvain), Louvain-la-Neuve 1348, Belgium;* orcid.org/0000-0001-7157-3197; Email: flavio.abreuaraujo@uclouvain.be

Authors

Oriane de Leuze – *Institute of Condensed Matter and Nanosciences (ICMN), Université catholique de Louvain (UCLouvain), Louvain-la-Neuve 1348, Belgium*

Michael Pohlitz – *Faculty of Physical Engineering/Computer Sciences, University of Applied Sciences Zwickau, Zwickau 08056, Germany*

Marco A. Villena – *Departamento de Electrónica y Tecnología de Computadores, Universidad de Granada, Facultad de Ciencias, Avenida de Fuentenueva s/n, Granada 18071, Spain;* orcid.org/0000-0001-5547-3380

Ramon Torres-Cavanillas – *Instituto de Ciencia Molecular, Universitat de Valencia, Valencia 46980, Spain;* orcid.org/0000-0002-3431-6113

Colin Ducarme – *Institute of Condensed Matter and Nanosciences (ICMN), Université catholique de Louvain (UCLouvain), Louvain-la-Neuve 1348, Belgium*

Anthony Lopes Temporao – *Institute of Condensed Matter and Nanosciences (ICMN), Université catholique de Louvain (UCLouvain), Louvain-la-Neuve 1348, Belgium*

Thomas G. Coppée – *Institute of Condensed Matter and Nanosciences (ICMN), Université catholique de Louvain (UCLouvain), Louvain-la-Neuve 1348, Belgium*

Anatole Moureaux – *Institute of Condensed Matter and Nanosciences (ICMN), Université catholique de Louvain (UCLouvain), Louvain-la-Neuve 1348, Belgium*

Sofiane Arib – *Institute of Condensed Matter and Nanosciences (ICMN), Université catholique de Louvain (UCLouvain), Louvain-la-Neuve 1348, Belgium*

Eugenio Coronado – *Instituto de Ciencia Molecular, Universitat de Valencia, Valencia 46980, Spain;* orcid.org/0000-0002-1848-8791

Christian Klaus Müller – *Faculty of Physical Engineering/Computer Sciences, University of Applied Sciences Zwickau, Zwickau 08056, Germany*

Juan Bautista Roldán – *Departamento de Electrónica y Tecnología de Computadores, Universidad de Granada, Facultad de Ciencias, Avenida de Fuentenueva s/n, Granada 18071, Spain;* orcid.org/0000-0003-1662-6457

Benoît Hackens – *Institute of Condensed Matter and Nanosciences (ICMN), Université catholique de Louvain*

(UCLouvain), Louvain-la-Neuve 1348, Belgium; orcid.org/0000-0001-6121-5126

Complete contact information is available at: https://pubs.acs.org/doi/10.1021/acsaelm.6c00766

Notes

The authors declare no competing financial interest.

■ ACKNOWLEDGMENTS

Research supported by the project PID2022-139586NB-C44, funded by MCIN/AEI/10.13039/501100011033 and FEDER, EU; and supported by the Ramón y Cajal grant (RYC2022-035618- I), funded by MCIU/AEI/10.13039/501100011033, and by the FSE+. F.A.A. is a Research Fellow of the F.R.S.-FNRS. C.K.M. thanks the Deutsche Forschungsgemeinschaft for funding (No. 531524052). The authors acknowledge funding from the EU (Pathfinder-4D-NMR 101099676), the Spanish MCIN (Unit of Excellence "Maria de Maeztu" CEX2019-000919-M). We are grateful for the funding provided by the Perte Chip Chairs of the Ministerio para la Transformación Digital y de la Función Pública, the European Union − NextGenerationEU. R.T-C. thanks the University of Valenciana for the Banc Santander grant (Santander UV25-23) and "la Caixa" Foundation (Neuron2Dblue).

■ REFERENCES

(1) Sebastian, R. K. A.; Le Gallo, M.; Eleftheriou, E. Memory Devices and Applications for In-Memory Computing. *Nat. Nanotechnol.* **2020**, *15* (7), 529−544.

(2) Shafiee, A.; Nag, A.; Muralimanohar, N.; Balasubramonian, R.; Strachan, J. P.; Hu, M.; Williams, R. S.; Srikumar, V. ISAAC: A Convolutional Neural Network Accelerator with In-Situ Analog Arithmetic in Crossbars. *ACM SIGARCH Comput. Archit. News* **2016**, *44* (3), 14−26.

(3) Backus, J. Can Programming Be Liberated from the von Neumann Style? A Functional Style and Its Algebra of Programs. *Commun. ACM* **1978**, *21* (8), 613−641.

(4) Zidan, M. A.; Strachan, J. P.; Lu, W. D. The Future of Electronics Based on Memristive Systems. *Nat. Electron.* **2018**, *1* (1), 22−29.

(5) Horowitz, M. Computing's Energy Problem (and What We Can Do about It). In *Proceedings of the IEEE International Solid-State Circuits Conference (ISSCC)*, **2014**, *57*, 10−14.

(6) Liu, L.; Li, Z.; Kang, H.; Xiao, Y.; Sun, L.; Zhao, H.; Zhu, Z. Q.; Ma, Y. Review of Surrogate Model Assisted Multi-Objective Design Optimization of Electrical Machines: New Opportunities and Challenges. *Renewable Sustainble Energy Rev.* **2025**, *215*, No. 115609.

(7) Attwell, D.; Laughlin, S. B. An Energy Budget for Signaling in the Grey Matter of the Brain. *J. Cereb. Blood Flow Metab.* **2001**, *21* (10), 1133−1145.

(8) Indiveri, G.; Liu, S.-C. Memory and Information Processing in Neuromorphic Systems. *Proc. IEEE* **2015**, *103* (8), 1379−1397.

(9) Chua, L. O. Memristor—The Missing Circuit Element. *IEEE Trans. Circuit Theory* **1971**, *18* (5), 507−519.

(10) Yang, J. J.; Strukov, D. B.; Stewart, D. R. Memristive Devices for Computing. *Nat. Nanotechnol.* **2013**, *8* (1), 13−24.

(11) Prezioso, F.; Merrikh-Bayat, M.; Hoskins, B. D.; Adam, G. C.; Likharev, K. K.; Strukov, D. B. Training and Operation of an Integrated Neuromorphic Network Based on Metal-Oxide Memristors. *Nature* **2015**, *521* (7550), 61−64.

(12) Waser, R.; Aono, M. Nanoionics-Based Resistive Switching Memories. *Nat. Mater.* **2007**, *6* (11), 833−840.

(13) Fuller, E. J.; Gabaly, F. E.; Léonard, F.; Agarwal, S.; Plimpton, S. J.; Jacobs-Gedrim, R. B.; James, C. D.; Marinella, M. J.; Talin, A. A. Li-Ion Synaptic Transistor for Low-Power Analog Computing. *Adv. Mater.* **2017**, *29* (4), No. 1604310.

(14) Solanki, A.; Guerrero, A.; Zhang, Q.; Bisquert, J.; Sum, T. C. Interfacial Mechanism for Efficient Resistive Switching in Ruddlesden−Popper Perovskites for Non-Volatile Memories. *J. Phys. Chem. Lett.* **2020**, *11* (2), 463−470.

(15) Sangwan, V. K.; Lee, H.-S.; Bergeron, H.; Balla, I.; Beck, M. E.; Chen, K.-S.; Hersam, M. C. Gate-Tunable Memristive Phenomena Mediated by Grain Boundaries in Single-Layer MoS_2. *Nat. Nanotechnol.* **2015**, *10* (5), 403−406.

(16) Avila, L. B.; Chulkin, P.; Serrano, P. A.; Dreyer, J. P.; Berteau-Rainville, M.; Orgiu, E.; França, L. D. L.; Zimmermann, L. M.; Bock, H.; Faria, G. C.; Eccher, J.; Bechtold, I. H. Perylene-Based Columnar Liquid Crystal: Revealing Resistive Switching for Nonvolatile Memory Devices. *J. Mol. Liq.* **2024**, *402*, No. 124757.

(17) Sawa, A. Resistive Switching in Transition Metal Oxides. *Mater. Today* **2008**, *11* (6), 28−36.

(18) Park, S.; Kim, H.; Jang, H. W. Device-Level Implementation of Reservoir Computing With Memristors. *Adv. Intell. Syst.* **2026**, *8*, No. e202500843.

(19) Xiang, K.; Song, J.; Liu, H.; Chen, J.; Yan, F. Organic Electrochemical Transistors for Neuromorphic Devices and Applications. *Adv. Mater.* **2026**, *38* (9), No. e15532.

(20) Liu, S.; Li, P.; Fu, X.; Zhou, K.; Ji, Y.; Zhao, B.; Di, D. Ionic Behaviors of Perovskite Devices and Their Neuromorphic Applications. *Adv. Funct. Mater.* **2026**, *36* (15), No. e10934.

(21) Zhou, Z.; Ma, Y.; Brezesinski, T.; Breitung, B.; Wu, Y.; Ma, Y. Improving upon Rechargeable Battery Technologies: On the Role of High-Entropy Effects. *Energy Environ. Sci.* **2025**, *18* (1), 19−52.

(22) Yu, J.; Duan, M.; Yang, G.; Jia, C. Gate-Tunable Resistive Switching and Negative Differential Resistance in Monolayer MoS_2 for Neuromorphic Computing. *ACS Appl. Electron. Mater.* **2025**, *7* (7), 7553−7561.

(23) Ma, J.; Liu, M.; He, Y.; Zhang, J. Iodine Redox Chemistry in Rechargeable Batteries. *Angew. Chem., Int. Ed.* **2021**, *60*, 12636.

(24) He, Q.; Lin, Z.; Ding, M.; Yin, A.; Halim, U.; Wang, C.; Liu, Y.; Cheng, H.-C.; Huang, Y.; Duan, X. In Situ Probing Molecular Intercalation in Two-Dimensional Layered Semiconductors. *Nano Lett.* **2019**, *19* (10), 6819−6826.

(25) Li, D.; Wang, D.; Tao, Y.; Zhang, S.; Ma, G.; Rao, Y.; Feng, C.; Liu, C.; Wan, H.; Wang, H. Memristors Based on Metal−Organic Frameworks: Synthesis, Mechanism, Categories, and Future. *ACS Appl. Electron. Mater.* **2025**, *7* (18), 8295−8321.

(26) Shu, F.; Chen, X.; Yu, Z.; Gao, P.; Liu, G. Metal−Organic Frameworks-Based Memristors: Materials, Devices, and Applications. *Molecules* **2022**, *27*, No. 8888.

(27) Park, J.; Im, E.; Park, S. The Chemistry and Role of Surface-Mounted Metal−Organic Frameworks (SURMOFs) in Next-Generation Nanoelectronics. *Coord. Chem. Rev.* **2025**, *540*, No. 216761.

(28) Abdullah, M.; Patil, A. R.; Patil, P. P.; Kamat, R. K.; Dongale, T. D.; Kim, T. G.; Arunachalam, K. P.; Kesavan, A. V. Zeolitic Imidazolate Framework-8 (ZIF-8)-Based Metal−Organic Framework for Neuromorphic Computing: Resistive Switching and Bio-Synaptic Characteristics. *Solid State Sci.* **2026**, *176*, No. 108286.

(29) Ide, M.; Sato, H.; Ozawa, H.; Haga, M.-A. Regulation of Ion Transport in Prussian Blue MOF Films by a Ru Complex Primer Nanolayer on an ITO Electrode and Its Energy Storage Application. *ACS Appl. Electron. Mater.* **2021**, *3* (9), 3962−3971.

(30) Avila, L. B.; Serrano, P. A.; Quispe, L. T.; Dantas, A.; Costa, D. P.; Arizaca, E. E. C.; Chávez, D. P. P.; Portugal, C. D. V.; Müller, C. K. Prussian Blue Anchored on Reduced Graphene Oxide Substrate Achieving High Voltage in Symmetric Supercapacitor. *Materials* **2024**, *17*, No. 3782.

(31) Zhang, B.; Zhang, J.; He, Y.; Zhou, K.; Wang, H. Recent Advances in Prussian Blue Analogues as Cathode Materials for Sodium-Ion Batteries. *J. Energy Chem.* **2025**, *110*, 593−615.

(32) Torres-Cavanillas, R.; Chen, H.; Castells-Gil, J.; Hidalgo, D.; Arenós-Amat, M.; Allen, C. S.; Fabi, G.; Gramse, G.; Coronado, E.;

Bogani, L. Synthesis of Large-Area 2D Prussian Blue as Ion-Transport Channels for Non-Volatile Memristors. *Small* **2026**, *22* (15), No. e12120.
(33) Buser, H. J.; Schwarzenbach, D.; Petter, W.; Ludi, A. The Crystal Structure of Prussian Blue: $Fe_4[Fe(CN)_6]_{3\cdot x}H_2O$. *Inorg. Chem.* **1977**, *16* (11), 2704−2710.
(34) Zhang, S.; Gao, S.; Zhang, Y.; Song, Y.; Gentle, I. R.; Wang, L.; Luo, B. All-Soluble All-Iron Aqueous Redox Flow Batteries: Towards Sustainable Energy Storage. *Energy Storage Mater.* **2025**, *75*, No. 104004 .
(35) Avila, L. B.; Müller, C. K.; Hildebrand, D.; Faita, F. L.; Baggio, B. F.; Cid, C. C. P.; Pasa, A. A. Resistive Switching in Electrodeposited Prussian Blue Layers. *Materials* **2020**, *13*, No. 5618.
(36) Avila, L. B.; Serrano Arambulo, P. C.; Dantas, A.; Cuevas-Arizaca, E. E.; Kumar, D.; Müller, C. K. Study on the Electrical Conduction Mechanism of Unipolar Resistive Switching Prussian White Thin Films. *Nanomaterials* **2022**, *12*, No. 2881.
(37) Lu, Y.; Zhang, J.; Chen, J.; Wang, W.; Liu, T.; Wei, L.; Wu, D.; You, B.; Zhang, W.; Qin, Y.; Shen, Y.; Du, J. Electric Control of Exchange Bias via Oxygen Ionic Migration in Co/NiO/Ta/HfO_2 Resistive Switching Devices. *ACS Appl. Electron. Mater.* **2025**, *7* (23), 10777−10785.
(38) Avila, L. B.; Cantudo, A.; Villena, M. A.; Maldonado, D.; Abreu Araujo, F.; Müller, C. K.; Roldán, J. B. Variability Analysis in Memristors Based on Electrodeposited Prussian Blue. *Microelectron. Eng.* **2025**, *300*, No. 112376.
(39) Cantudo, A.; Avila, L. B.; Villena, M. A.; Jiménez-Molinos, F.; Ducarme, C.; Lopes Temporao, A.; Moureaux, A.; Abreu Araujo, F.; Müller, C. K.; Roldán, J. B. Conductance Quantization in Memristive Devices with Electrodeposited Prussian Blue-Based Dielectrics. *Mater. Sci. Semicond. Process.* **2026**, *203*, No. 110253.
(40) Palacios-Corella, M.; Echevarria, I.; Santana Santos, C.; Schuhmann, W.; Ventosa, E.; Ibáñez, M. Prussian Blue Analogues as Anode Materials for Battery Applications: Complexities and Horizons. *Chem. Mater.* **2025**, *37* (12), 4203−4226.
(41) Aluru, N. R.; Darling, S. B.; Elam, J. W.; Gang, O.; Salleo, A.; Siwy, Z.; Talin, A. A.; Noy, A. Knowledge Gaps for Neuromorphic Ionic Computing. *Science* **2026**, *392* (6798), 592−601.
(42) Pezhumkattil Palakkal, J.; Lekshmi, P. N.; Thomas, S.; Valant, M.; Suresh, K. G.; Varma, M. R. Polarons Induced Electronic Transport, Dielectric Relaxation and Magnetodielectric Coupling in Spin Frustrated Ba_2FeWO_6. *Mater. Res. Bull.* **2016**, *76*, 161−168.
(43) Hegner, F. S.; Galán-Mascarós, J. R.; López, N. A Database of Structural and Electronic Properties of Prussian Blue Compounds. *Inorg. Chem.* **2016**, *55* (24), 12851−12862.
(44) Pei, Q.; Heeger, A. J. Operating Mechanism of Light-Emitting Electrochemical Cells. *Nat. Mater.* **2008**, *7* (3), 167−168.
(45) Tang, S.; Sandström, A.; Lundberg, P.; Lanz, T.; Larsen, C.; van Reenen, S.; Kemerink, M.; Edman, L. Design Rules for Light-Emitting Electrochemical Cells Delivering Bright Luminance at 275 Percent External Quantum Efficiency. *Nat. Commun.* **2017**, *8*, No. 1190.
(46) Faita, F. L.; Avila, L. B.; Silva, J. P. B.; Boratto, M. H.; Plá Cid, C. C.; Graeff, C. F. O.; Gomes, M. J. M.; Müller, C. K.; Pasa, A. A. Abnormal Resistive Switching in Electrodeposited Prussian White Thin Films. *J. Alloys Compd.* **2022**, *896*, No. 162971.
(47) Vazirisereshk, M. R.; Sumaiya, S. A.; Chen, R.; Baykara, M. Z.; Martini, A. Time-Dependent Electrical Contact Resistance at the Nanoscale. *Tribol. Lett.* **2021**, *69*, No. 50.
(48) Yuan, Y.; Lanza, M. The Effect of Relative Humidity in Conductive Atomic Force Microscopy. *Adv. Mater.* **2024**, *36*, No. 2405932.
(49) Lim, E. W.; Ismail, R. Conduction Mechanism of Valence Change Resistive Switching Memory: A Survey. *Electronics* **2015**, *4*, 586−613.
(50) Villeneuve-Faure, C.; Boumaarouf, A.; Shah, V.; Gammon, P. M.; Lüders, U.; Coq Germanicus, R. SiC Doping Impact during Conducting AFM under Ambient Atmosphere. *Materials* **2023**, *16*, No. 5401.
(51) Reid, O. G.; Munechika, K.; Ginger, D. S. Space-Charge-Limited Current Measurements Using Conductive AFM. *Nano Lett.* **2008**, *8* (6), 1602−1609.
(52) Zivasatienraj, B.; Tellekamp, M. B.; Weidenbach, A. S.; Ghosh, A.; McCrone, T. M.; Doolittle, W. A. Temporal Versatility from Intercalation-Based Neuromorphic Devices Exhibiting 150 mV Non-Volatile Operation. *J. Appl. Phys.* **2020**, *127* (8), No. 084501.
(53) Mai, V. H.; Moradpour, A.; Senzier, P. A.; Pasquier, C.; Wang, K.; Rozenberg, M. J.; Giapintzakis, J.; Orfanidou, C. M.; Svoukis, E.; Breza, A.; Lioutas, C. B.; Franger, S.; Revcolevschi, A.; Maroutian, T.; Lecoeur, P.; Aubert, P.; Agnus, G.; Salot, R.; Albouy, P. A.; Weil, R.; Alamarguy, D.; March, K.; Jomard, F.; Chrétien, P.; Schneegans, O. Memristive and Neuromorphic Behavior in a Li_xCoO_2 Nanobattery. *Sci. Rep.* **2015**, *5*, No. 7761.
(54) Choi, Y.; Lee, C.; Kim, M.; Song, Y.; Hwang, H.; Lee, D. Structural Engineering of Li-Based Electronic Synapse for High Reliability. *IEEE Electron Device Lett.* **2019**, *40* (12), 1992−1995.
(55) Sasaki, T.; Ukyo, Y.; Novák, P. Memory Effect in a Lithium-Ion Battery. *Nat. Mater.* **2013**, *12*, 569−575.
(56) Ioannou, P. S.; Kyriakides, E.; Schneegans, O.; Giapintzakis, J. Evidence of Biorealistic Synaptic Behavior in Diffusive Li-Based Two-Terminal Resistive Switching Devices. *Sci. Rep.* **2020**, *10*, No. 8711.
(57) Kim, S. J.; Kim, S.; Jang, H. W. Competing Memristors for Brain-Inspired Computing. *iScience* **2021**, *24*, No. 101889.
(58) Milano, G.; Luebben, M.; Ma, Z.; Dunin-Borkowski, R.; Boarino, L.; Pirri, C. F.; Waser, R.; Ricciardi, C.; Valov, I. Self-Limited Single Nanowire Systems Combining All-in-One Memristive and Neuromorphic Functionalities. *Nat. Commun.* **2018**, *9*, No. 5151.
(59) Lim, B. M.; Lee, Y. M.; Yoo, C. S.; Kim, M.; Kim, S. J.; Kim, S.; Yang, J. J.; Lee, H.-S. High-Reliability and Self-Rectifying Alkali Ion Memristor through Bottom Electrode Design and Dopant Incorporation. *ACS Nano* **2024**, *18* (8), 6373−6386.
(60) Wang, X.; Guo, Z.; Zheng, W.; Liu, Z.; Liu, T.; Chen, X.; Cai, P.; Zhang, Q.; Liao, W. Resistive Switching Behaviors and Conduction Mechanisms of IGZO/ZnO Bilayer Heterostructure Memristors. *APL Mater.* **2024**, *12* (11), No. 111105.
(61) He, Y.; Ting, Y.-Y.; Hu, H.; Diemant, T.; Dai, Y.; Lin, J.; Schweidler, S.; Marques, G. C.; Hahn, H.; Ma, Y.; Brezesinski, T.; Kowalski, P. M.; Breitung, B.; Aghassi-Hagmann, J. Printed High-Entropy Prussian Blue Analogs for Advanced Non-Volatile Memristive Devices. *Adv. Mater.* **2025**, *37*, No. 2410060.